

A SINGLE ADDITIVE FOR 3D PRINTING OF HIGHLY-CONCENTRATED IRON OXIDE INKS

by  
AMIN HODAEI

Submitted to the Graduate School of Engineering and Natural Sciences  
in partial fulfillment of  
the requirements for the degree of  
Master of Science

Sabanci University  
January 2018

TITLE OF THE THESIS/DISSERTATION

"A single additive for 3D printing of highly-concentrated iron oxide inks"

APPROVED BY:

Asst. Prof. Dr.  
(Thesis Supervisor)

Handwritten signature in blue ink, appearing to read "Ezra Alverdim" with a checkmark above the name.

Prof. Dr.

Handwritten signature in blue ink, appearing to read "Behlül Koc" with a checkmark above the name.

Assoc. Prof. Dr.

Handwritten signature in blue ink, appearing to read "Ezra ALVERDIM" with a checkmark above the name.

DATE OF APPROVAL: 05/01/2018

© Amin Hodaei 2018

All Rights Reserved

## ABSTRACT

### A SINGLE ADDITIVE FOR 3D PRINTING OF HIGHLY-CONCENTRATED IRON OXIDE INKS

Amin Hodaei

Master's Thesis, January 2018

Supervisor: Assist. Prof. Ozge Akbulut

Keywords: 3D printing, iron oxide, colloids, magnetic nanoparticles, inductors, suspensions

A single additive, a grafted copolymer, is designed to prepare highly-loaded suspensions of iron oxide nanoparticles (IOPs) and to facilitate the extrusion-based 3D printing of these stable suspensions. This poly (ethylene glycol) (PEG)-grafted copolymer of N-[3(dimethylamino)propyl]methacrylamide (DMAPMA) and acrylic acid (AA) harnesses both electrostatic and steric repulsion to realize an optimum formulation for 3D printing of IOP inks. With the use of 1.15 wt. % (by the weight of IOPs), the suspension attains ~81 wt. % solid loading—96% of the theoretical limit as calculated by the Krieger-Dougherty equation. We fabricated rectangular, thick-walled toroidal, and thin-walled toroidal magnetic cores and a porous lattice structure to demonstrate the utilization of this ink for 3D printing. The electrical and magnetic properties of the magnetic cores were characterized through impedance spectroscopy (IS) and vibrating sample magnetometry (VSM), respectively. The IS indicated the possibility of utilizing wire-wound 3D printed cores as the inductive coils. The VSM confirmed the magnetic properties of IOPs before and after the ink formulation were kept almost unchanged due to the low loading of the additive. This particle-targeted approach for the

formulation of 3D printing inks realizes the embodiment of a fully aqueous system with utmost target material content.

## OZET

# YÜKSEK KONSANTRASYONLU DEMİR OKSİT MÜREKKEPLERİNİN 3D BASKISI İÇİN TEK BİR KATKI

Amin Hodaei

Master's Thesis, January 2018

Supervisor: Assist. Prof. Ozge Akbulut

Keywords: 3D baskı, demir oksit, kolloidler, manyetik nanopartiküller, indüktörler, süspansiyonlar

Tek bir katkı maddesi, graflanmış bir kopolimer, demir oksit nanopartiküllerinin (DON'lerin) aşırı yüklü süspansiyonlarını hazırlamak ve bu sebatlı süspansiyonların ekstrüzyon temelli 3D baskısını kolaylaştırmak üzere tasarlanmıştır. Bu poli (etilen glikol) (PEG) graflanmış N- [3 (dimetilamino) propil] metakrilamidin (DMPMA) ve akrilik asitin (AA) kopolimeri, DON mürekkeplerinin 3D baskısı için optimum bir formülasyonu gerçekleştirmek için hem elektrostatik hem de sterik itmeyi harekete geçirir. Ağırlıkça 1.15 wt. % (DON'lerin ağırlığı ile), süspansiyon ağırlıkça yaklaşık% 81'e ulaşır. Katı yükleme oranı - Krieger-Dougherty denklemi ile hesaplanan teorik sınırın% 96'sı. Üç boyutlu baskı için bu mürekkebin kullanımını göstermek için dikdörtgen, kalın duvarlı toroidal ve ince cidarlı toroidal manyetik çekirdekler ve gözenekli bir kafes yapısı imal ettik. Manyetik çekirdeklerin elektriksel ve manyetik özellikleri, sırasıyla, empedans spektroskopisi (IS) ve titreşimli numune manyetometresi (VSM) ile karakterize edildi. IS, endüktif bobinler olarak telle sarılmış 3D baskılı çekirdeklerin kullanılma ihtimalini belirtti. VSM, mürekkep formülasyonunun, katkı maddesinin düşük yüklenmesi nedeniyle neredeyse hiç değişmeden tutulduktan ve sonrasında DON'lerin manyetik özelliklerini doğrulamıştır. 3D baskı mürekkeplerin formülasyonu için bu parçacık hedefli yaklaşım, en yüksek hedef madde içeriğine sahip tamamen sulu bir sistemin gerçekleştirir.

## ACKNOWLEDGEMENTS

I would like to express my sincere gratitude to my advisor, Prof. Ozge Akbulut, for the continuous support of my Master's and related studies, for her guidance, encouragement and immense knowledge.

My special thanks go to Prof. Yusuf Menciloglu, Dean of the Faculty of Engineering and Natural Sciences, for his support and constructive comments and also the Faculty of Engineering and Natural Sciences for providing this opportunity which allowed me to undertake this research.

Finally, I would like to thank my parents and my sister for supporting me spiritually throughout my Master's and my life in general.

## TABLE OF CONTENT

Chapter 1 A single additive enables 3D printing of highly-loaded iron oxide suspensions	7
1.1 Introduction .....	7
1.2 Characterization of the additives .....	9
1.3 Design of chemical and structural properties of the additives .....	12
Chapter 2 Electro-kinetic behavior and adsorption study.....	13
Chapter 3 Rheological characterizations .....	16
Chapter 4 3D printing of the IOP ink and characterization of its magnetic and electrical properties.....	21
4.1 Conclusion .....	26
Chapter 5 Reference .....	27
Chapter 6 Experimental Section .....	30
6.1 Materials .....	30
6.2 Synthesis and characterization of the additives .....	30
6.2.1 Synthesis of the additives .....	30
6.2.2 Characterization of the additives .....	31
6.3 Preparation and 3D printing of highly-loaded iron oxide inks.....	31
6.3.1 Ink formulation.....	31
6.3.2 3D printing of highly-loaded iron oxide inks .....	31
6.3.3 Electro-kinetic study and adsorption behavior of the additives .....	32
6.3.4 Rheological study.....	32
6.3.5 Potentiometric titration of the solutions of the additives .....	33
6.3.6 Studying the interaction of the additives with Fe <sup>3+</sup> Ions .....	33
6.3.7 Field emission scanning electron microscopy (FESEM) .....	33
6.3.8 Impedance spectroscopy.....	33
6.3.9 Magnetic characterization.....	33

## LIST OF FIGURES

Figure 1.1. The general chemical structure of the additives.....	9
Figure 1.2 a) $^1\text{H}$ NMR and b) $^{13}\text{C}$ NMR spectra of the P10 additive in $\text{D}_2\text{O}$ (The wide peak at $\sim 5$ 4.8 ppm originates from the solvent ( $\text{D}_2\text{O}$ ) in the $^1\text{H}$ NMR measurement) .	13
Figure 2.1. Zeta potential of IOPs as a function of change in the pH of the medium .....	13
Figure 2.2. a) Zeta potential of IOPs in the presence of the additives, and b) Adsorption behavior of the additives onto the surface of IOPs as a function of polymer loading (dotted lines show 100% adsorption).....	15
Figure 3.1. a) Viscosity change in the 55 wt. % IOP suspensions in the presence of 1 wt. % of different additives, b) The change in the viscosity of the suspensions of IOPs in the presence of 1–1.3 wt. % P10, c) The viscosity as a function of shear rate response of IOP inks at different particle loadings in the presence of the optimum amount of P10 (1.15 wt. %), d) Oscillatory rheological measurements (frequency = 10 rad s $^{-1}$ ) of IOP inks of different particle loadings ranging from 55 wt. % to $\sim 81$ wt. %, and e) The yield stress of the IOP inks assigned as the crossover of $G'$ and $G''$ curves (the dotted line shows the transition from shear to plug flow region)..	19
Figure 3.2. Dependency of viscosity on the volume fraction of IOPs in the presence of 1.15 wt.% of P10 .....	20
Figure 4.1. 3D printing of the magnetic cores, a) Thick-walled toroidal, b) Thin-walled toroidal, and c) Rectangular shapes; d) Dried cores after printing, e) One-layer thick pattern of “SU” letters, f) A porous structure, and g) SEM micrograph of the fractured surface of the porous structure that is shown in “f”. Scale bars are a) 10 mm, b) 10 mm, c) 5 mm, d) 5 mm, e) 5 mm, f) 10 $\mu\text{m}$ (left), and 1 $\mu\text{m}$ (right) .....	21
Figure 4.2. a) The photos of the room temperature dried 3D printed cores before wire winding; b) Rectangular, c) Thick-walled toroidal and d) Thin-walled toroidal cores wound with 60 turns of wire, and e) The connection of the wire-wound thick-walled core to the outlets of the impedance spectrometer .....	22
Figure 4.3. Room temperature magnetic hysteresis (M–H) loops of the bare IOPs and the dried sample of the ink that is used for printing .....	23
Figure 4.4. a) The frequency response of the inductance, b) The change in the resistance as a function of frequency, and c) The frequency dependence of the quality factors of the inductors with 60 turns of wire .....	24

## Chapter 1 A single additive enables 3D printing of highly-loaded iron oxide suspensions

This chapter is written based on the submitted article “A single additive enables 3d printing of highly-loaded iron oxide suspensions”. A series of a poly (ethylene glycol) (PEG)-grafted copolymer of N-[3(dimethylamino)propyl]methacrylamide (DMAPMA) and acrylic acid (AA) were synthesized to harness both electrostatic and steric repulsion in iron oxide nanoparticles (IOPs) colloidal system for the realization of an optimum formulation for 3D printing. With the use of 1.15 wt. % (by the weight of IOPs) of the optimum additive, the suspension attains ~81 wt. % IOP loading.

### 1.1 Introduction and Motivation

3D printing has demonstrated its potential to realize functionality along with form;<sup>1, 2</sup> and has gone beyond prototyping and found several applications in energy storage/conversion,<sup>3, 4</sup> microfluidics,<sup>5-7</sup> electronics,<sup>8-11</sup> and building hierarchical structures.<sup>12, 13</sup> The extrusion-based printing of metallic and ceramic colloidal systems is a branch of 3D printing, where highly concentrated suspensions of particles (40–55 vol. %)<sup>14</sup> are extruded to build near-net shaped structures with complex geometries.<sup>2</sup> The extrusion-based 3D printing of ceramics and metals necessitates inks with controlled rheological properties to enable proper deposition through a nozzle and to ensure shape retention of the extrusion thereafter.<sup>15</sup> Up to date, there are only a few number of metallic (e.g., silver<sup>16-18</sup>) and ceramic (e.g., silicon carbide,<sup>19</sup> alumina,<sup>20</sup> and barium titanate<sup>21</sup>) colloidal systems that have been printed through this process. To form a shape retaining filament usually polymeric binders (e.g., poly(vinyl butyral)<sup>22</sup>), dispersants (e.g., poly(acrylic acid)<sup>23</sup> and ammonium polyacrylates<sup>24</sup>), and surfactants (e.g., dimethyl methyl phosphonate<sup>25</sup> and butyric acid<sup>26</sup>) are used. These formulations rely mostly on the electrostatic repulsion for providing the stability and controlling the printing parameters of the suspensions. Moreover, there is a single report that employed a comb type copolymer, thus combined steric hindrance with electrostatic repulsion to formulate an ink of alumina.<sup>20</sup> The studies on the stability of colloidal systems emphasize the benefit of utilizing both electrostatic and steric repulsion,<sup>27, 28</sup> however, the application of this knowledge to 3D printing has not yet been fully achieved. The limited portfolio of printable materials can be potentially expanded by employing a particle-specific design, which exploits both types of repulsion,

to attain rheology controlled inks.<sup>14</sup>

Large-area magnets,<sup>29</sup> transformers,<sup>30</sup> magnets with complex shapes,<sup>31</sup> constant-flux inductors,<sup>32</sup> and electrochemical devices<sup>33</sup> can be realized with magnetic inks. Until now, polymer-based composites of Neodymium Iron Boron (NdFeB) family,<sup>29, 31, 33</sup> iron,<sup>30, 32</sup> and NiCuZn ferrite<sup>32</sup> are the only magnetic inks that have been used in extrusion-based 3D printing. These inks have been formulated by using high amounts of additives (5–8 wt. %<sup>32</sup> to ~69 wt. %, calculated<sup>33</sup>) which lowers the loading of the magnetic particles and limits the performance of fabricated objects by reducing the magnetic material filling factor.<sup>34</sup> To be utilized as inks, polymer-based magnetic composites require heating to impart flowability to the system. These heat treatment steps might be detrimental for certain magnetic materials such as iron oxide ( $\text{Fe}_3\text{O}_4$ ) which goes through a phase transition at 200 °C resulting in changing its magnetic properties.<sup>35</sup>

Herein, the preparation and 3D printing of highly-loaded iron oxide ( $\text{Fe}_3\text{O}_4$ ) inks through the minimum use of a single additive that is specifically designed for iron oxide nanoparticles is reported. Iron oxide is a soft magnetic material with relatively high saturation magnetization, low electrical conductivity, high permeability, and easy magnetization/demagnetization properties which make it a candidate material for applications such as the cores of inductive coils,<sup>36</sup> drug delivery systems,<sup>37</sup> and wastewater treatment.<sup>38</sup> A particle-specific approach was pursued to design an additive that can cater the surface charge and its distribution in IOPs and can provide both electrostatic and steric repulsion to stabilize and tailor the viscosity of the suspensions of IOPs. We synthesized poly(ethylene glycol) (PEG)-grafted copolymers of N-[3(dimethylamino)propyl]methacrylamide (DMAPMA) and acrylic acid (AA) and studied the effect of i) comonomer ratios, and ii) the density of PEG side chains on the stability of the IOPs suspensions. The optimized ink contained ~81 wt. % of IOPs in the presence of 1.15 wt. % of a single additive (by weight of IOPs) in an aqueous medium. To demonstrate the printability of various geometries, three different shapes of magnetic cores (rectangular, thick-walled toroidal, and thin-walled toroidal cores) and a porous lattice structure were printed. The electrical and magnetic properties of the cores were systematically characterized through impedance spectroscopy (IS) and vibrating sample magnetometry (VSM), respectively. To the best of our knowledge, this fully aqueous ink is the first of its

kind for extrusion-based 3D printing in terms of the magnetic material of choice at highest amounts through the minimum use of a single additive.

Our motivation to conduct this research was to propose a solution for the expansion of the limited portfolio of the ceramic inks used in 3D printing. These inks have been usually made in the presence of multiple additives and non-fully aqueous systems to reach high concentrations of the targeted materials. Our method suggests a facile and green route to formulate highly-concentrated iron oxide inks as a member of ceramic materials to construct cores of the inductors in addition to geometrically complex shapes.

## 1.2 Characterization of the additives

All the additives were synthesized by aqueous free radical polymerization of acrylic acid (AA), N-[3(dimethylamino)propyl] methacrylamide (DMAPMA), and esterified-PEG-1000. The esterification of PEG-1000 by maleic anhydride (MA) was carried out via the procedure that was proposed by Lu et al..<sup>39</sup> The general chemical structure of the additives is shown in Figure 1.1.

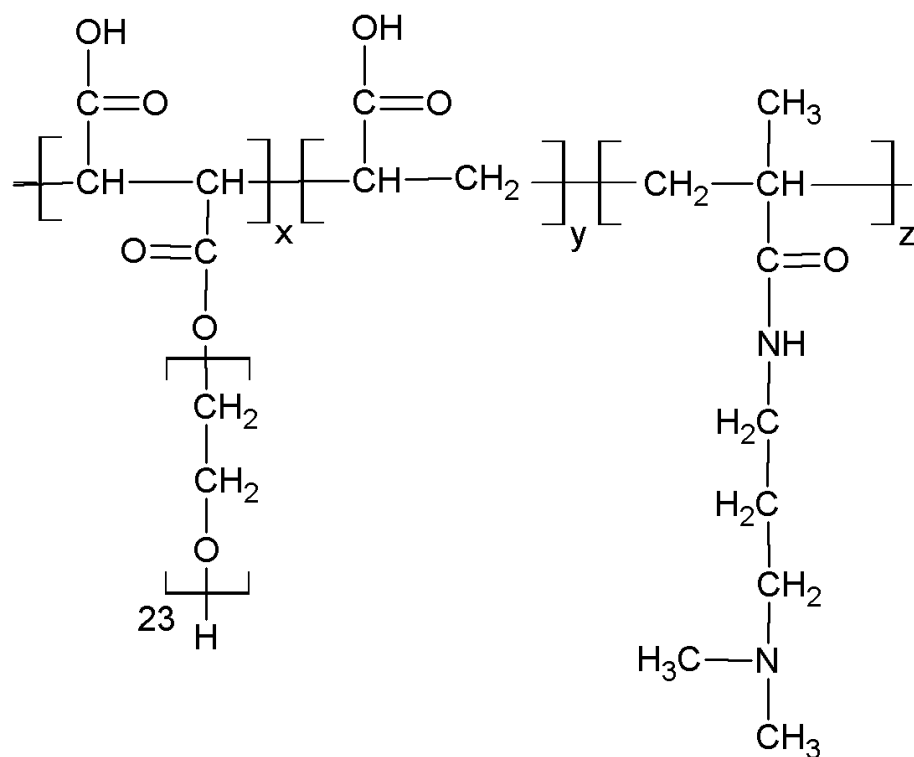


Figure 1.1. The general chemical structure of the additives.

The molar ratios of the building blocks incorporated into the structure of the additives were determined by  $^1\text{H}$ -NMR and the related data are listed in Table 1.1. Charge density of the copolymers were calculated from direct addition of NaOH to polymer solution by titration. The compositions of the grafted copolymers were tracked by  $^1\text{H}$  NMR and  $^{13}\text{C}$  NMR and the composition of the additive P10 is shown in Figure 1.2.

Table 1.1. The molar feed ratios and the characteristic properties of the synthesized additives.

Polymer acronym	Molar feed ratio (DMAPMA/AA/PEG)	DMAPM A/AA <sup>a)</sup>	PEG/(DMAPMA+A) <sup>a)</sup>	mmol anionic sites per mg of solid <sup>b)</sup>	Molecular weight ( $M_w$ ) (g/mol) <sup>c)</sup>	PDI ( $M_w/M_n$ )
DMA50	50:0:1	–	0.27/50	N/A	21,685	1.49
DMA40	40:10:1	0.95	0.82/50	$4.7 \times 10^{-3}$	24,832	1.53
DMA30	30:20:1	0.93	0.90/50	$4.9 \times 10^{-3}$	37,471	1.86
DMA25	25:25:1	0.72	0.42/50	$5.9 \times 10^{-3}$	63,668	2.33
DMA20	20:30:1	0.98	0.41/50	$4.4 \times 10^{-3}$	196,740	2.99
P5	25:25:5	0.88	1.74/50	$5.6 \times 10^{-3}$	56,570	1.63
P10	25:25:10	0.97	2.87/50	$5.3 \times 10^{-3}$	32,449	1.19

<sup>a)</sup> Determined by  $^1\text{H}$  NMR; <sup>b)</sup> Calculated from direct addition of NaOH to the solutions of additives by titration; <sup>c)</sup> Measured by gel permeation chromatography.

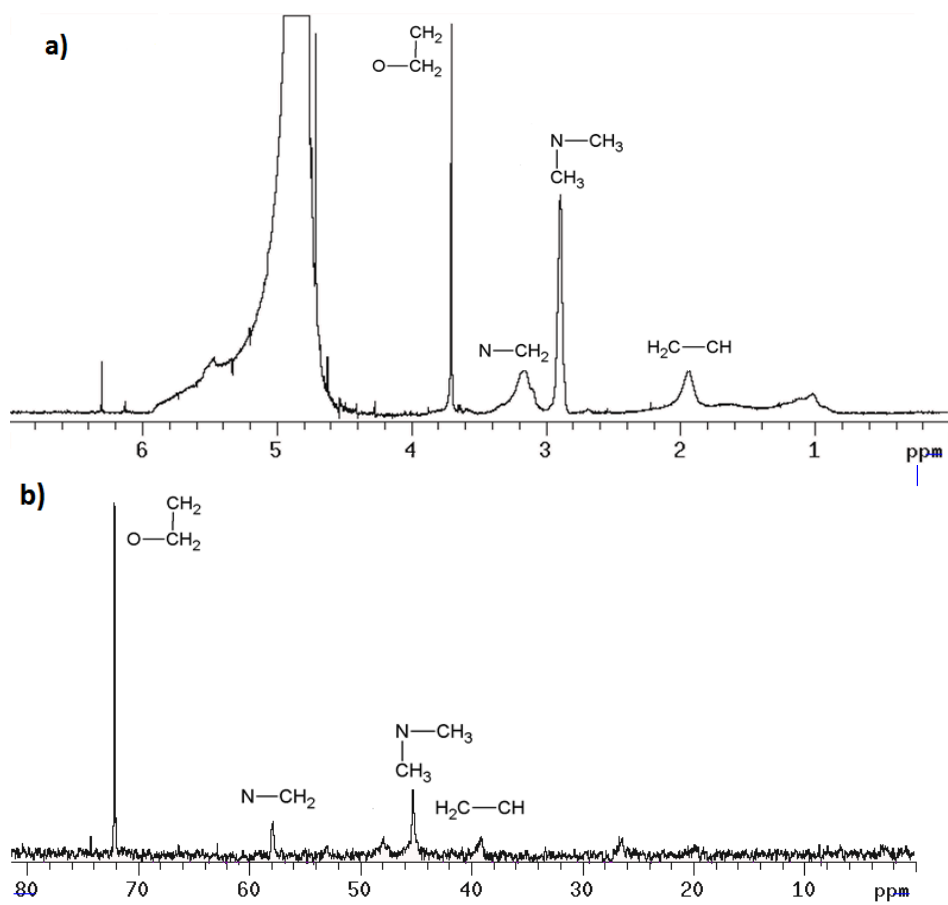


Figure 1.2 a) <sup>1</sup>H NMR and b) <sup>13</sup>C NMR spectra of the P10 additive in D<sub>2</sub>O (The wide peak at ~4.8 ppm originates from the solvent (D<sub>2</sub>O) in the <sup>1</sup>H NMR measurement).

### 1.3 Design of Chemical and Structural Properties of the Additives

The surface of IOPs bears hydroxyl moieties<sup>40</sup> which can facilitate the attachment of chemical agents with certain functional groups (e.g. amine, carboxylic acid, etc.).<sup>41, 42</sup> IOPs have been usually stabilized with the aid of homopolymeric additives such as PEG,<sup>43</sup> dextran,<sup>44</sup> poly(vinyl alcohol),<sup>45</sup> poly(ethyleneimine),<sup>46</sup> poly(vinylpyrrolidone),<sup>47</sup> and poly(acrylic acid).<sup>48</sup> A few systems with copolymers, for instance, poly(2-vinylpyridine-*g*-acrylic acid),<sup>49</sup> poly(2-acrylamido-2-methyl-1-propanesulfonic acid-*co*-acrylic acid),<sup>50</sup> polyamidoamine-*graft*-poly(ethylene glycol)/dodecyl amine,<sup>51</sup> and poly(vinyl alcohol-*co*-vinyl amine)<sup>52</sup> have also been investigated. In this work, DMAPMA, which is a polar monomer that contains a tertiary amine functional group, was chosen as one of the backbone monomers. Tertiary amine groups act as proton acceptors and lone pair donors (Brønsted and Lewis bases),<sup>53</sup> and in an aqueous medium, they can be protonated by receiving protons from water.<sup>54</sup> Moreover, alkyl groups that are attached to nitrogen atom stabilize its positive charge.<sup>55</sup> The amine functional group adsorbs onto the surface of IOPs via electrostatic interactions.<sup>56</sup> The other comonomer, AA, bears a carboxylic acid functional group that has a strong complexation ability with the surface of iron oxide.<sup>57</sup> As *grafts*, we have used maleic anhydride esterified PEG (MAPEG) due to its water solubility. The molar feeding ratios of the building blocks are listed in Table 1 and the compositions of the grafted copolymers were tracked by <sup>1</sup>H NMR and <sup>13</sup>C NMR (Figure 1.2a and 1.2b). The amount of AA was increased to find the optimum ratio of DMAPMA/AA in the additives (DMA50 to DMA20, hereafter referred to as DMA series). Moreover, the feeding molar ratio of PEG side chains was raised to track the steric hindrance effect of the additives. The ratio of DMAPMA/AA and the characteristic properties of the grafted copolymers are shown in Table 1.1 columns 3–7.

## Chapter 2 Electro-kinetic Behavior and Adsorption Study

Electro-kinetic behavior of nanoparticles (NPs) is a feature of assessing their stability in suspensions. The presence of additives can alter the interparticle forces of suspensions through the change in Zeta potential of the host particles upon adsorption.<sup>58</sup> The electro-kinetic behavior of the IONPs through measuring their Zeta potential changes at different aqueous medium pH values and in the presence of varying amounts of additives were tracked (Figure 2.1 and 2.2). The hydroxyl functional groups on the surface IOPs can be protonated/deprotonated depending on the pH of the medium resulting in the change of surface charge of the NPs.<sup>40</sup> The bare IOPs showed a negative Zeta potential of  $\sim -29$  mV at pH 7.2 (Figure 2.1).

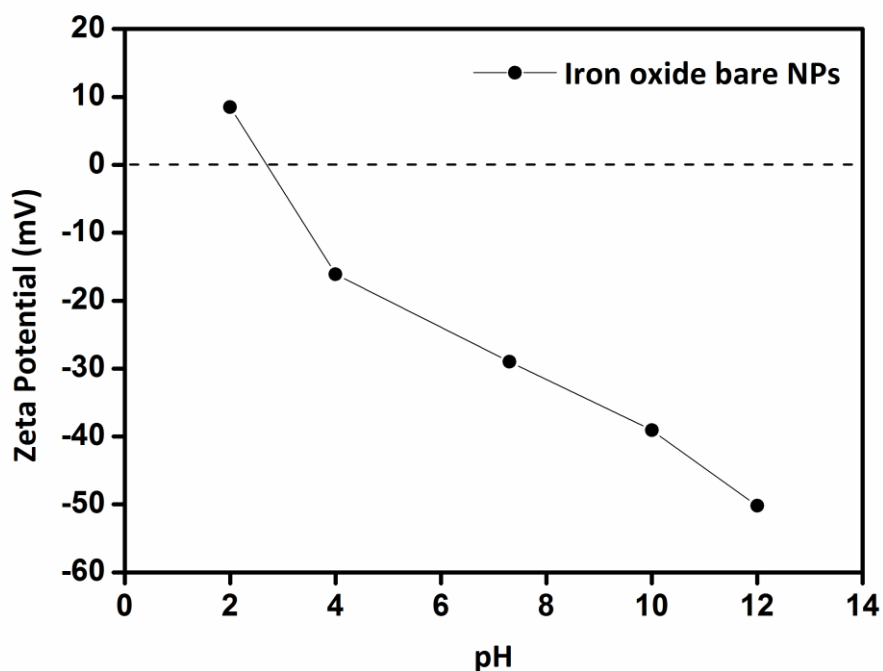


Figure 2.1. Zeta potential of IOPs as a function of change in the pH of the medium.

Upon adsorption of all the additives at low dosages, Zeta potential of the bare IOPs increased from  $\sim -29$  mV to positive values ( $+20$  mV  $<$ ) and reached a plateau region at higher dosages of the additives ( $\geq \sim 0.8$  wt. %) (Figure 2.2a). Zeta potential values of  $> +30$  or  $< -30$  mV ensure the electrostatic stability of the colloidal systems.<sup>59</sup> The Zeta potential of the bare IOPs was more significantly changed in the presence of DMA25 compared to

the other additives in DMA series. Thus, this feeding ratio of the backbone comonomers was chosen to investigate the performance of the additives with higher density of the side chains. The grafted copolymers DMA25, P5, and P10 (in increasing amount of the side chains and equal amounts of the comonomers in the backbone) changed the Zeta potentials from  $\sim -29$  mV to above  $\sim +37$  mV. Compared to DMA25, P5, and P10 showed relatively lower plateau values of Zeta potential. This phenomenon may be attributed to the shielding of charge-containing layer of the adsorbed additives on the surface of the IOPs by the steric effect of higher side chain population of P5 and P10 compared to that of DMA25.<sup>60</sup>

The adsorption isotherms were studied to clarify the effect of AA on the change of Zeta potential of IOPs and the adsorption behavior of the additives. The amount of the additives adsorbed on the IOPs firstly increased, and then saturated near a plateau value which is typical for a monolayer adsorption isotherm (Figure 2.2b).<sup>61</sup> While the slope of the initial range is attributed to the affinity of the additives to the surface of IOPs, the plateau value is correlated to the complete coverage of IOPs by additives.<sup>62</sup> Among DMA series, DMA25, which contains higher proportion of AA comonomer in the backbone (Table 1.1), demonstrates higher affinity of adsorption as well as adsorption saturation (see Figure 2.2b). Generally, AA is a weak acid with strong complexation towards multivalent cations. These carboxylate moieties can form different complexations such as monodentate, bidentate, and binuclear complexes with the surface of IOPs.<sup>63</sup> Inductively coupled plasma optical emission spectrometry (ICP-OES) revealed that the complexation ability of the additives is directly related to the content of AA comonomer in the backbone (Table 1.1 column 3 and Table 2.1). Thus, higher adsorption tendency of DMA25 compared to that of other DMA series can be correlated to the higher complexation of this additive with iron species at the surface of IOPs.<sup>64</sup> The  $\text{Fe}^{3+}$  ions complexation with the additives was studied by inductively coupled plasma optical emission spectrometry (ICP-OES) (See Table 2.1).

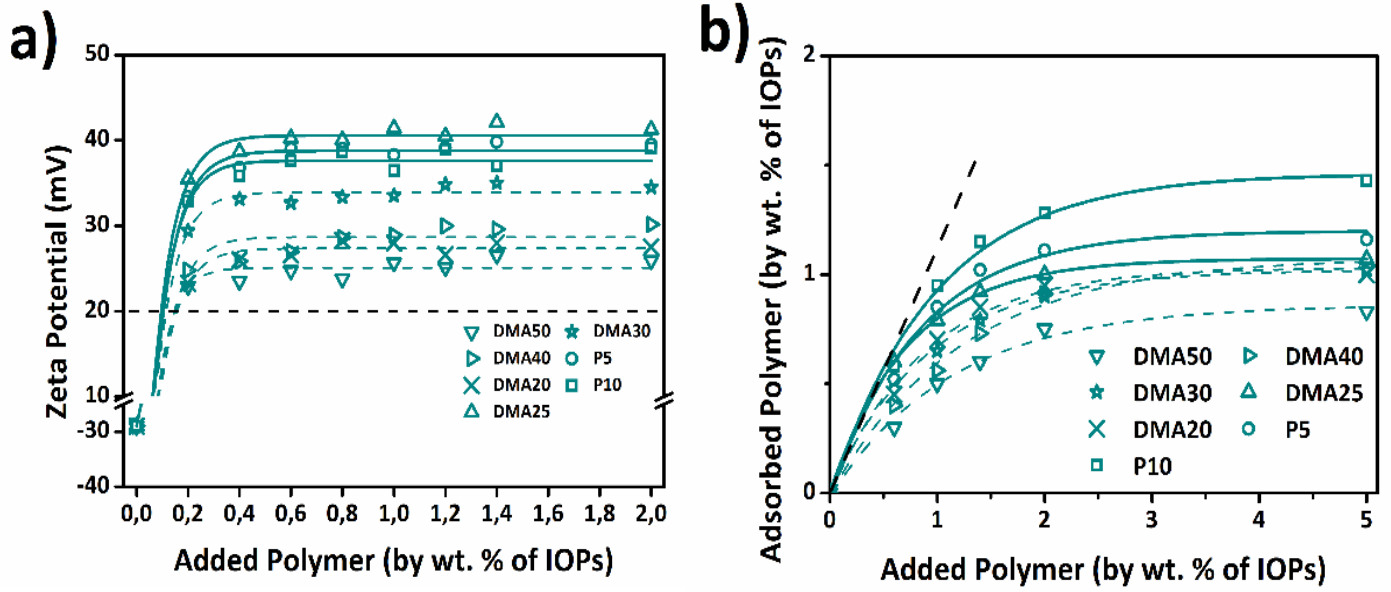


Figure 2.2. a) Zeta potential of IOPs in the presence of the additives, and b) Adsorption behavior of the additives onto the surface of IOPs as a function of polymer loading (dotted lines show 100% adsorption).

Table 2.1. The measured  $\text{Fe}^{3+}$  concentration complexed with the additives in aqueous solutions.

<b>Polymer acronym</b>	<b><math>[\text{Fe}^{3+}]</math> complexed with the additives (ppm)</b>
DMA50	0.0
DMA40	2.5
DMA30	3.1
DMA25	11.3
DMA20	3.5
P5	3.7
P10	3.9

### Chapter 3 Rheological Characterization

The rheological response of the inks for extrusion-based 3D printing should be tailored to i) achieve a filamentary shape upon flow through the deposition nozzle<sup>65</sup> and ii) to prevent deformation of the printed patterns after extrusion and sagging of the filaments<sup>66</sup>. The rheological parameters of the inks that should be controlled for extrusion-based 3D printing include i) apparent viscosity, ii) yield stress, and viscoelastic behaviors (i.e. the elastic and loss moduli)<sup>67</sup>. To achieve a shape-forming extrusion upon deposition<sup>65</sup> and to prevent deformation and sagging of the printed patterns after extrusion,<sup>66</sup> the rheological response of the inks at different loadings of IOPs and additives by measuring their apparent viscosity, yield stress, and loss and elastic moduli was evaluated.

In the absence of any additives, the maximum loading of the IOPs was determined as ~55 wt. %. The viscosity measurements were firstly conducted on the 55 wt. % IOPs suspensions in the presence of 1 wt. % of the additives. This dosage is the value at which the Zeta potential of IOPs in the presence of all additives has reached its plateau and is the starting point of the plateau region in the adsorption isotherms of all the additives (Figure 3.1a and 3.1b). All the suspensions exhibited shear-thinning behavior—decrease in the viscosity of suspension with increasing the shear rate, while the suspension that contains P10 had the lowest level of viscosity among all samples (see Figure 3.1a). This behavior is an indication of the higher potential of P10 compared to those of the other additives to provide an ink formulation with higher IOP loading. Considering Zeta potential (Figure 2.2a), adsorption isotherms (Figure 2.2b), and the viscosity response as a function of shear rate (Figure 3.1a), P10 was singled out for further studies.

To avoid inadequate or excess addition of the additives, the amount of P10 was optimized by investigating the change in the viscosity of 55 wt. % suspensions with different amounts of the additive (1–1.3 wt. %) as a function of shear rate. The viscosity of suspensions decreased with additive dosage up to 1.15 wt. % and it increased beyond this content exhibiting an optimum loading at 1.15 wt. % to achieve a highly-dispersed suspension (see Figure 3.1b).

The viscosity and the viscoelastic properties of the suspensions with varying IOP loadings and the optimum loading of the additive (1.15 wt. %) was monitored to assess the printability of highly-concentrated suspensions (Figure 3.1c and 3.1d). Increasing the loading of IOPs from 55 to 81 wt. % in the presence of the optimum dosage of the additive, the viscosity of the suspensions increased by more than three orders of magnitude in the shear rate range of 0.01–100 s<sup>-1</sup>. Moreover, all the samples showed shear-thinning behavior (see Figure 2c). Additionally, they demonstrated an elastic behavior (i.e., storage modulus ( $G'$ ) > loss modulus ( $G''$ ) by almost two orders of magnitude) up to the crossover point of the storage and loss moduli ( $G'=G''$ ) (Figure 3.1d).

The stress at the crossover of  $G'$  and  $G''$  is assigned as the yield stress of the suspensions.<sup>68</sup> The yield stress of the suspensions is a measure for determining the suitability of a given nozzle geometry for the formation of extrudate in 3D printing. If the yield stress exceeds the maximum shear stress at the wall of the nozzle, the ink enters a plug flow regime where the flow behavior of the ink and its subsequent extrudate formation is

hard to control.<sup>68</sup> Therefore, the critical condition for the most suitable shear flow during 3D printing was determined using Equation (1):<sup>69</sup>

$$\tau = \left(\frac{\Delta P}{2L}\right)r \quad (1)$$

where  $\Delta P$  (Pa) is the maximum pressure applied at the nozzle,  $r$  (m) is the radius of the nozzle, and  $L$  (m) is the length of the nozzle. The maximum shear stress at the wall of the nozzle was calculated as 1657.5 Pa through inserting the parameters ( $\Delta P = 195$  kPa,  $r = 255$   $\mu\text{m}$ , and  $L = 15$  mm) that are used in this work into Equation (1). By the increase in the loading of IOPs from 55 wt. % to  $\sim 81$  wt. %, the yield stress of the suspensions changed from 9.7 to 984.5 Pa (Figure 2d)—the yield stress of the ink with  $\sim 81$  wt. % loading of IOPs was still below the stress that will cause the plug flow (Figure 3.1e). This value is close to the maximum loading of IOPs in the suspensions,  $\sim 84.4$  wt.%, as calculated by the Krieger–Dougherty model. Hence, we chose the ink with the highest IOP loading,  $\sim 81$  wt. %, for the 3D printing of the magnetic cores (Figure 3.2).

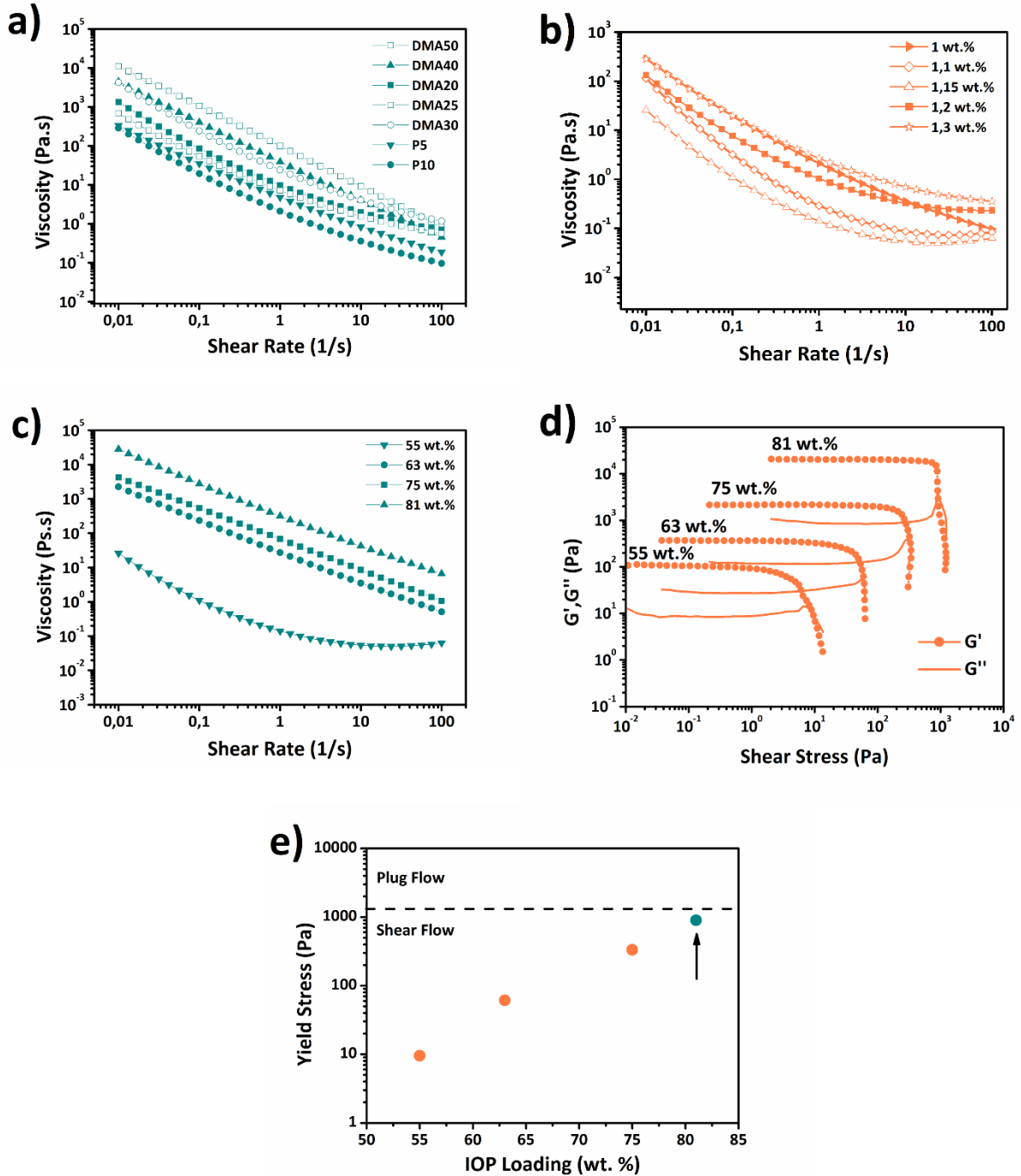


Figure 3.1. a) Viscosity change in the 55 wt. % IOP suspensions in the presence of 1 wt. % of different additives, b) The change in the viscosity of the suspensions of IOPs in the presence of 1–1.3 wt. % P10, c) The viscosity as a function of shear rate response of IOP inks at different particle loadings in the presence of the optimum amount of P10 (1.15 wt. %), d) Oscillatory rheological measurements (frequency =  $10 \text{ rad s}^{-1}$ ) of IOP inks of different particle loadings ranging from 55 wt. % to ~81 wt. %, and e) The yield stress of the IOP inks assigned as the crossover of  $G'$  and  $G''$  curves (the dotted line shows the transition from shear to plug flow region).

Krieger–Dougherty model was utilized to find the maximum loading of IOPs in the suspensions according to the following equation:<sup>70</sup>

$$\mu = \mu_0 \left(1 - \frac{\phi}{\phi_{\max}}\right)^{-\left(\frac{\mu}{\phi_{\max}}\right)} \quad (1)$$

where  $\mu$  is the viscosity of the suspension (Pa.s),  $\mu_0$  is the viscosity of the media (Pa.s),  $\phi_{\max}$  is the maximum particle loading (vol. %) attainable for a system. Using the IOPs loadings and the viscosities of their aqueous suspensions (in the presence of the optimum amount of P10 (1.15 wt. %)) in the Krieger–Dougherty model at the shear rate of  $1 \text{ s}^{-1}$  resulted in a value of 51.4 vol. % ( $\sim 84.4 \text{ wt. \%}$ ) as  $\phi_{\max}$ . The empirical maximum solid loading achieved in the ink formulations ( $\sim 81 \text{ wt. \%}$ ) is 96 % of the maximum possible loading of IOPs ( $\sim 84.4 \text{ wt. \%}$ ) according to the Krieger-Dougherty model.

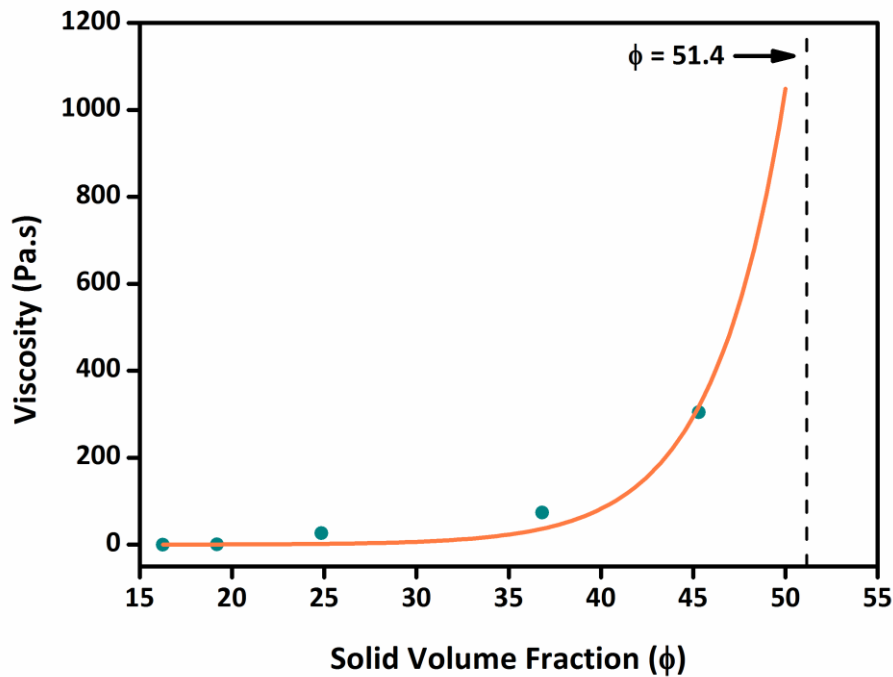


Figure 3.2. Dependency of viscosity on the volume fraction of IOPs in the presence of 1.15 wt.% of P10.

## Chapter 4 3D Printing of the IOP ink and characterization of its magnetic and electrical properties

Three different shapes of the magnetic cores were 3D printed: i) rectangular shape of  $24 \times 5 \times 3$  mm, ii) thin-walled, and thick-walled toroidal shapes of  $20 \times 18 \times 12$  and  $16 \times 8 \times 8$  mm (outer diameter  $\times$  inner diameter  $\times$  height), respectively, and iii) a porous lattice structure (Figure 4.1).

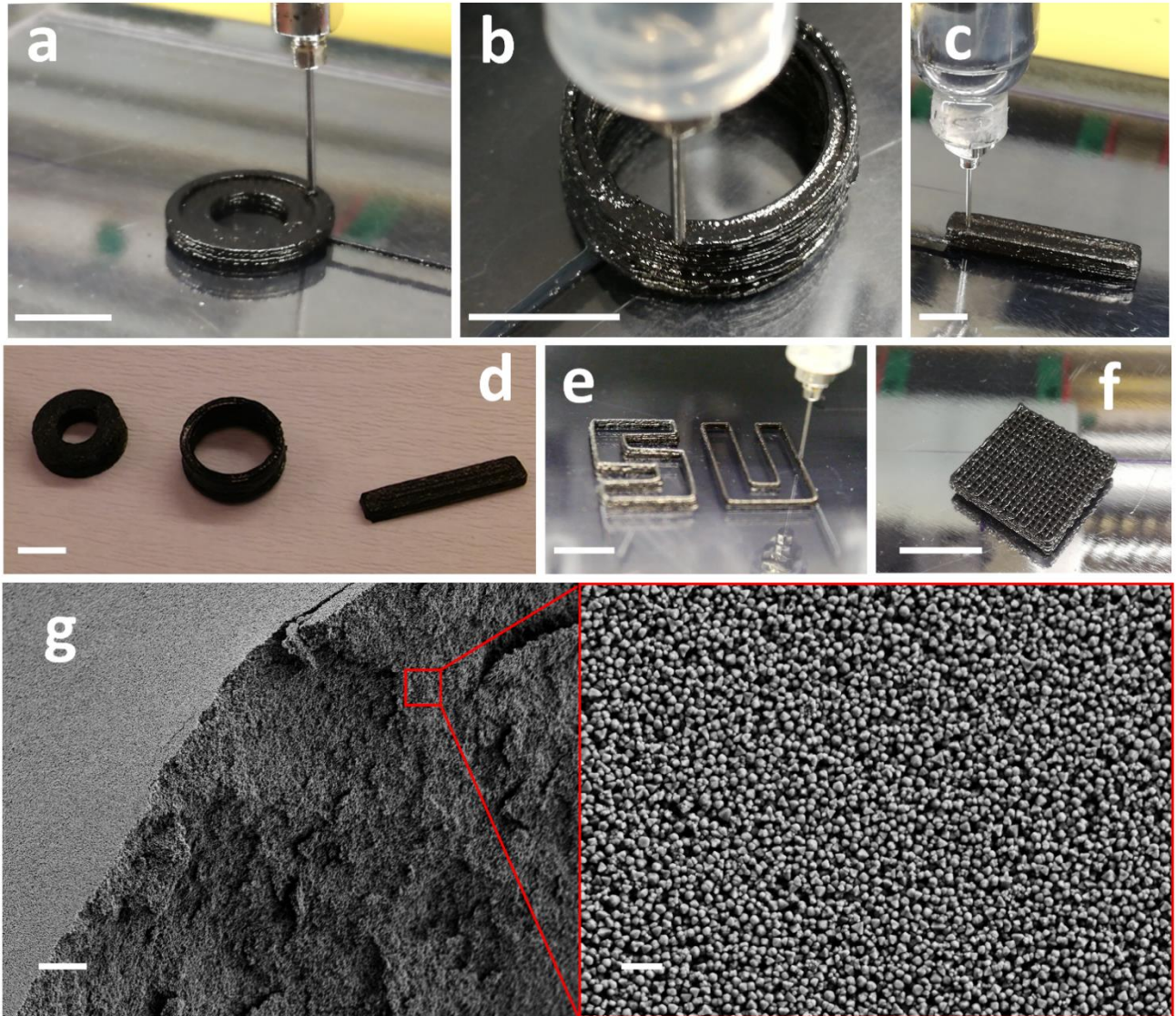


Figure 4.1. 3D printing of the magnetic cores, a) Thick-walled toroidal, b) Thin-walled toroidal, and c) Rectangular shapes; d) Dried cores after printing, e) One-layer thick pattern of “SU” letters, f) A porous structure, and g) SEM micrograph of the fractured surface of the porous structure that is shown in “f”. Scale bars are a) 10 mm, b) 10 mm, c) 5 mm, d) 5 mm, e) 5 mm, f) 10 mm, g) 10  $\mu$ m (left), and 1  $\mu$ m (right).

The printed cores were wire-wound with 60 turns of 0.2 mm thick (for thin-walled toroidal shape) and 0.3 mm thick (for rectangular and thick-walled toroidal shapes) copper wires (See Figure 4.2).

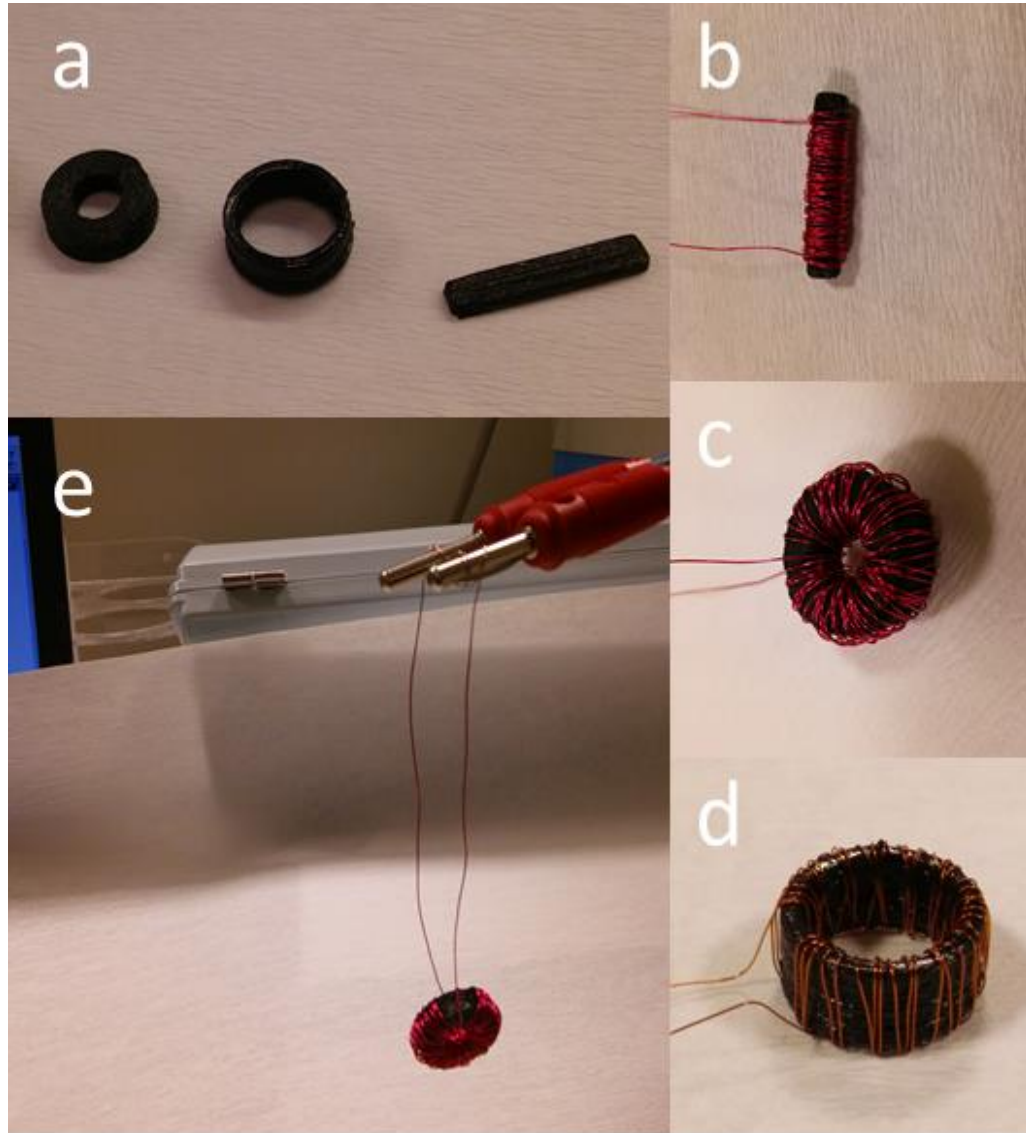


Figure 4.2. a) The photos of the room temperature dried 3D printed cores before wire winding; b) Rectangular, c) Thick-walled toroidal and d) Thin-walled toroidal cores wound with 60 turns of wire, and e) The connection of the wire-wound thick-walled core to the outlets of the impedance spectrometer.

To compare the magnetic properties of the bare IOPs and the ink used for 3D printing, the room temperature magnetic hysteresis (M–H) loops of the as-received particles and the dried sample of the ink (containing ~81 wt. % IOPs with the presence of 1.15 wt. % of P10) were measured (see Figure 4.3). Both samples demonstrated quite the same magnetic behavior, constructed narrow (M–H) loops, and reached a saturation magnetization which is typical for the soft magnetic materials.<sup>71</sup> This observation clarifies that the magnetic behavior of the nanoparticles is not affected by the ink formulation that is used in this study.

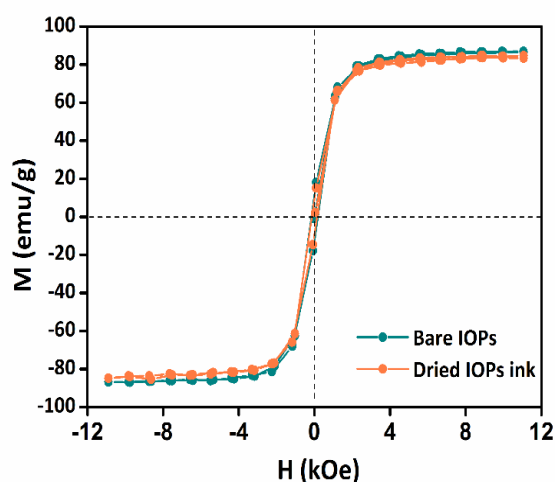


Figure 4.3. Room temperature magnetic hysteresis (M–H) loops of the bare IOPs and the dried sample of the ink that is used for printing.

The electrical behavior of the wire-wound cores was tracked by measuring the inductance and resistance of the inductors as a function of frequency (0.1 MHz–10 MHz) by impedance spectroscopy (Figures 4.4a and 4.4b). Generally, soft magnetic materials are used as the materials of the cores of the inductors to increase the inductance.<sup>72</sup> Expectedly, the inductance of all the inductors was enhanced due to the coupling between the wire turns wound around the magnetic cores. However, inductance decreased by increasing the frequency; this phenomenon can be attributed to factors such as electrical currents induced in the cores (eddy-current loss), displacement currents in the cores, and magnetic hysteresis losses.<sup>73</sup> Moreover, the resistance of the inductors increased with frequency up to 10 MHz. This increase is attributed to the skin effect and proximity effect as the other sources of loss.<sup>74</sup>

To investigate the performance of the inductors as electrical components, the quality factor (Q) of the inductors, a measure of efficiency, was calculated using the Equation (2):<sup>75</sup>

$$Q = \frac{2\pi fL}{R_s} \quad (2)$$

where L is inductance (H),  $R_s$  is series resistance ( $\Omega$ ), and f is the frequency of operation (Hz) (Figure 4.4c).

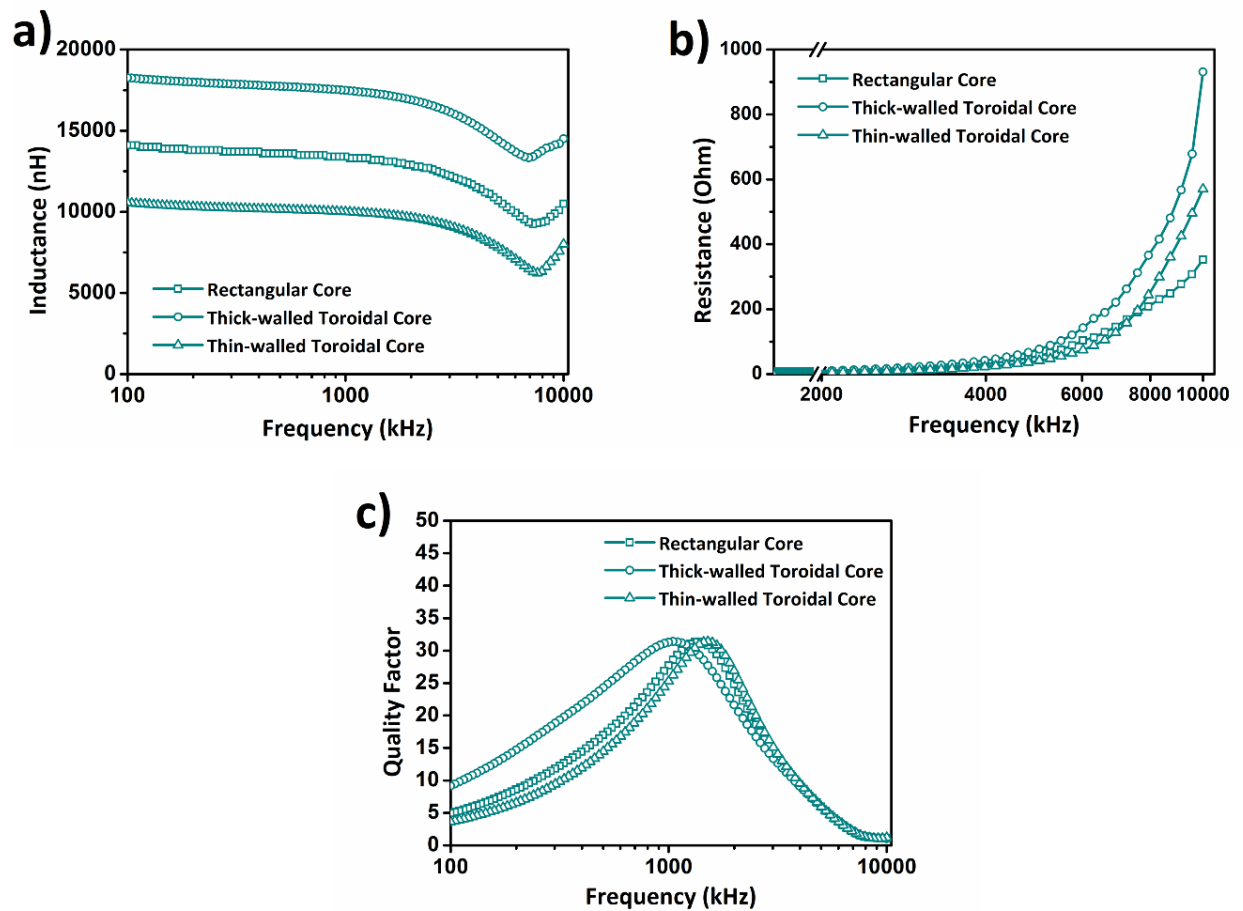


Figure 4.4. a) The frequency response of the inductance, b) The change in the resistance as a function of frequency, and c) The frequency dependence of the quality factors of the inductors with 60 turns of wire.

For all the inductors, Q showed peaks at  $\sim 31$ . The change of maximum values of Q depends on the sources of resistance (i.e., the losses of the core and the losses of the wound wires). Since the material of the cores ( $\text{Fe}_3\text{O}_4$ ) and the wires (copper) were the same for all the inductors, observation of similar values for the peak of Qs was expected. The thick-walled toroidal core inductor delivered higher Q values compared to that of the other cores at a relatively broader range of frequency; thus, possessed a wider operating range of frequency. In summary, these inductor setups indicated that there is a high potential to manufacture magnetic cores in various geometries through 3D printing, which can find different applications in the wide realm of the electronic and electromechanical systems.

## **Chapter 4.1 Conclusion**

Highly-loaded suspensions, as inks for 3D printing, can only be achieved through careful tailoring of additives that can cater the properties of each type of the particle. The level of loading that is attained in this work eliminates the need for material removal steps and offers, for the first time in literature, a magnetic ink that contains highest loadings of particles with minimum amount of a single additive. In addition, this fully aqueous system has the potential to pave the way for domestic printing of ceramics. The particle-specific approach that is described for iron oxide provides a solid route to expand the limited portfolio of 3D printing inks.

## Chapter 5 Reference

1. N. Hopkinson, R. Hague and P. Dickens, in *Rapid Manufacturing: An industrial Revolution for the Digital Age*, John Wiley & Sons, Ltd, 2006, DOI: 10.1002/0470033991.ch1, pp. 1-4.
2. N. Travitzky, A. Bonet, B. Dermeik, T. Fey, I. Filbert-Demut, L. Schlier, T. Schlordt and P. Greil, *Advanced Engineering Materials*, 2014, **16**, 729-754.
3. K. Sun, T.-S. Wei, B. Y. Ahn, J. Y. Seo, S. J. Dillon and J. A. Lewis, *Advanced Materials*, 2013, **25**, 4539-4543.
4. R. R. Kohlmeyer, A. J. Blake, J. O. Hardin, E. A. Carmona, J. Carpena-Nunez, B. Maruyama, J. Daniel Berrigan, H. Huang and M. F. Durstock, *Journal of Materials Chemistry A*, 2016, **4**, 16856-16864.
5. W. Shen, M. Li, C. Ye, L. Jiang and Y. Song, *Lab on a Chip*, 2012, **12**, 3089-3095.
6. A. K. Au, W. Huynh, L. F. Horowitz and A. Folch, *Angewandte Chemie International Edition*, 2016, **55**, 3862-3881.
7. P. J. Kitson, M. H. Rosnes, V. Sans, V. Dragone and L. Cronin, *Lab on a Chip*, 2012, **12**, 3267-3271.
8. Y. L. Kong, I. A. Tamargo, H. Kim, B. N. Johnson, M. K. Gupta, T.-W. Koh, H.-A. Chin, D. A. Steingart, B. P. Rand and M. C. McAlpine, *Nano Letters*, 2014, **14**, 7017-7023.
9. B. Y. Ahn, E. B. Duoss, M. J. Motala, X. Guo, S.-I. Park, Y. Xiong, J. Yoon, R. G. Nuzzo, J. A. Rogers and J. A. Lewis, *Science*, 2009, **323**, 1590-1593.
10. J. T. Muth, D. M. Vogt, R. L. Truby, Y. Mengüç, D. B. Kolesky, R. J. Wood and J. A. Lewis, *Advanced Materials*, 2014, **26**, 6307-6312.
11. A. Frutiger, J. T. Muth, D. M. Vogt, Y. Mengüç, A. Campo, A. D. Valentine, C. J. Walsh and J. A. Lewis, *Advanced Materials*, 2015, **27**, 2440-2446.
12. A. Clausen, F. Wang, J. S. Jensen, O. Sigmund and J. A. Lewis, *Advanced Materials*, 2015, **27**, 5523-5527.
13. E. B. Duoss, T. H. Weisgraber, K. Hearon, C. Zhu, W. Small, T. R. Metz, J. J. Vericella, H. D. Barth, J. D. Kuntz, R. S. Maxwell, C. M. Spadaccini and T. S. Wilson, *Advanced Functional Materials*, 2014, **24**, 4905-4913.
14. J. A. Lewis, *Current Opinion in Solid State and Materials Science*, 2002, **6**, 245-250.
15. J. H. Kim, S. Lee, M. Wajahat, H. Jeong, W. S. Chang, H. J. Jeong, J.-R. Yang, J. T. Kim and S. K. Seol, *ACS Nano*, 2016, **10**, 8879-8887.
16. R.-Z. Li, A. Hu, T. Zhang and K. D. Oakes, *ACS Applied Materials & Interfaces*, 2014, **6**, 21721-21729.
17. B. Y. Ahn, D. J. Lorange and J. A. Lewis, *Nanoscale*, 2011, **3**, 2700-2702.
18. N. Zhou, C. Liu, J. A. Lewis and D. Ham, *Advanced Materials*, 2017, **29**, 1605198-n/a.
19. C. M. Larson, J. J. Choi, P. A. Gallardo, S. W. Henderson, M. D. Niemack, G. Rajagopalan and R. F. Shepherd, *Advanced Engineering Materials*, 2016, **18**, 39-45.
20. X. Wang, Y. Sun, C. Peng, H. Luo, R. Wang and D. Zhang, *ACS Applied Materials & Interfaces*, 2015, **7**, 26131-26136.
21. S. S. Nadkarni and J. E. Smay, *Journal of the American Ceramic Society*, 2006, **89**, 96-103.
22. H. Yang, S. Yang, X. Chi and J. R. G. Evans, *Journal of Biomedical Materials Research Part B: Applied Biomaterials*, 2006, **79B**, 116-121.
23. Q. Li and J. A. Lewis, *Advanced Materials*, 2003, **15**, 1639-1643.
24. L. Sun, S. T. Parker, D. Syoji, X. Wang, J. A. Lewis and D. L. Kaplan, *Advanced Healthcare Materials*, 2012, **1**, 729-735.
25. B. G. Compton and J. A. Lewis, *Advanced Materials*, 2014, **26**, 5930-5935.

26. J. T. Muth, P. G. Dixon, L. Woish, L. J. Gibson and J. A. Lewis, *Proceedings of the National Academy of Sciences*, 2017, **114**, 1832-1837.
27. A. R. Studart, E. Amstad and L. J. Gauckler, *Langmuir*, 2007, **23**, 1081-1090.
28. L. Qi, J. Fresnais, P. Muller, O. Theodoly, J. F. Berret and J. P. Chapel, *Langmuir*, 2012, **28**, 11448-11456.
29. L. Li, A. Tirado, I. C. Nlebedim, O. Rios, B. Post, V. Kunc, R. R. Lowden, E. Lara-Curzio, R. Fredette, J. Ormerod, T. A. Lograsso and M. P. Paranthaman, *Scientific Reports*, 2016, **6**, 36212.
30. L. M. Bollig, P. J. Hilpisch, G. S. Mowry and B. B. Nelson-Cheeseman, *Journal of Magnetism and Magnetic Materials*, 2017, **442**, 97-101.
31. C. Huber, C. Abert, F. Bruckner, M. Groenefeld, O. Muthsam, S. Schuschnigg, K. Sirak, R. Thanhoffer, I. Teliban, C. Vogler, R. Windl and D. Suess, *Applied Physics Letters*, 2016, **109**, 162401.
32. Y. Yan, L. Liu, C. Ding, L. Nguyen, J. Moss, Y. Mei and G.-Q. Lu, 2017.
33. A. J. Bhandarkar, C. S. López, A. M. Vinu Mohan, L. Yin, R. Kumar and J. Wang, *Science Advances*, 2016, **2**.
34. H. Yun, X. Liu, T. Paik, D. Palanisamy, J. Kim, W. D. Vogel, A. J. Viescas, J. Chen, G. C. Papaefthymiou, J. M. Kikkawa, M. G. Allen and C. B. Murray, *ACS Nano*, 2014, **8**, 12323-12337.
35. J. A. Cuenca, K. Bugler, S. Taylor, D. Morgan, P. Williams, J. Bauer and A. Porch, *Journal of Physics: Condensed Matter*, 2016, **28**, 106002.
36. N. A. Spaldin, *Magnetic Materials: Fundamentals and Applications*, Cambridge University Press, New York, 2010.
37. M. Liong, J. Lu, M. Kovoichich, T. Xia, S. G. Ruehm, A. E. Nel, F. Tamanoi and J. I. Zink, *ACS Nano*, 2008, **2**, 889-896.
38. Y. F. Shen, J. Tang, Z. H. Nie, Y. D. Wang, Y. Ren and L. Zuo, *Separation and Purification Technology*, 2009, **68**, 312-319.
39. S.-H. Lu, G. Liu, Y.-F. Ma and F. Li, *Journal of Applied Polymer Science*, 2010, **117**, 273-280.
40. E. Illés and E. Tombácz, *Colloids and Surfaces A: Physicochemical and Engineering Aspects*, 2003, **230**, 99-109.
41. C. Boyer, M. R. Whittaker, V. Bulmus, J. Liu and T. P. Davis, *NPG Asia Mater*, 2010, **2**, 23-30.
42. S. Laurent, D. Forge, M. Port, A. Roch, C. Robic, L. Vander Elst and R. N. Muller, *Chemical Reviews*, 2008, **108**, 2064-2110.
43. C. Flesch, Y. Unterfinger, E. Bourgeat-Lami, E. Duguet, C. Delaite and P. Dumas, *Macromolecular Rapid Communications*, 2005, **26**, 1494-1498.
44. R. S. Molday and D. Mackenzie, *Journal of immunological methods*, 1982, **52**, 353-367.
45. J. Lee, T. Isobe and M. Senna, *Journal of Colloid and Interface Science*, 1996, **177**, 490-494.
46. X. Wang, L. Zhou, Y. Ma, X. Li and H. Gu, *Nano Research*, 2009, **2**, 365-372.
47. J. Huang, L. Bu, J. Xie, K. Chen, Z. Cheng, X. Li and X. Chen, *ACS Nano*, 2010, **4**, 7151-7160.
48. Y.-W. Choi, H. Lee, Y. Song and D. Sohn, *Journal of Colloid and Interface Science*, 2015, **443**, 8-12.
49. M. Billing, C. Gräfe, A. Saal, P. Biehl, J. H. Clement, S. Dutz, S. Weidner and F. H. Schacher, *Macromolecular Rapid Communications*, 2017, **38**, 1600637-n/a.
50. H. G. Bagaria, Z. Xue, B. M. Neilson, A. J. Worthen, K. Y. Yoon, S. Nayak, V. Cheng, J. H. Lee, C. W. Bielawski and K. P. Johnston, *ACS Applied Materials & Interfaces*, 2013, **5**, 3329-3339.

51. J. Chen, M. Shi, P. Liu, A. Ko, W. Zhong, W. Liao and M. M. Q. Xing, *Biomaterials*, 2014, **35**, 1240-1248.
52. A. Petri-Fink, B. Steitz, A. Finka, J. Salaklang and H. Hofmann, *European Journal of Pharmaceutics and Biopharmaceutics*, 2008, **68**, 129-137.
53. P. Navarro-Vega, Zizumbo-L, #xf3, A. pez, A. Licea-Claverie, A. Vega-Rios and F. Paraguay-Delgado, *Journal of Nanomaterials*, 2014, **2014**, 14.
54. V. Froidevaux, C. Negrell, S. Caillol, J.-P. Pascault and B. Boutevin, *Chemical Reviews*, 2016, **116**, 14181-14224.
55. S. A. Lawrence, *Amines: synthesis, properties and applications*, Cambridge University Press, 2004.
56. S. Seifert, F. Simon, G. Baumann, M. Hietschold, A. Seifert and S. Spange, *Langmuir*, 2011, **27**, 14279-14289.
57. B. Gu, T. L. Mehlhorn, L. Liang and J. F. McCarthy, *Geochimica et Cosmochimica Acta*, 1996, **60**, 1943-1950.
58. A. Zingg, F. Winnefeld, L. Holzer, J. Pakusch, S. Becker and L. Gauckler, *Journal of Colloid and Interface Science*, 2008, **323**, 301-312.
59. P. Somasundaran, *Encyclopedia of surface and colloid science*, CRC press, 2006.
60. J. Plank and B. Sachsenhauser, *Cement and Concrete Research*, 2009, **39**, 1-5.
61. R. I. Masel, *Principles of adsorption and reaction on solid surfaces*, John Wiley & Sons, 1996.
62. M. d. M. Alonso, M. Palacios and F. Puertas, *Industrial & Engineering Chemistry Research*, 2013, **52**, 17323-17329.
63. R. M. Cornell and U. Schwertmann, *The iron oxides: structure, properties, reactions, occurrences and uses*, John Wiley & Sons, 2003.
64. K.-C. Hsu, K.-L. Ying, L.-P. Chen, B.-Y. Yu and W.-C. J. Wei, *Journal of the American Ceramic Society*, 2005, **88**, 524-529.
65. A. R. Studart, *Chemical Society Reviews*, 2016, **45**, 359-376.
66. A. Zocca, P. Colombo, C. M. Gomes and J. Günster, *Journal of the American Ceramic Society*, 2015, **98**, 1983-2001.
67. J. A. Lewis and G. M. Gratson, *Materials Today*, 2004, **7**, 32-39.
68. G. Siqueira, D. Kokkinis, R. Libanori, M. K. Hausmann, A. S. Gladman, A. Neels, P. Tingaut, T. Zimmermann, J. A. Lewis and A. R. Studart, *Advanced Functional Materials*, 2017, **27**, 1604619-n/a.
69. S. James, *Editorial Willy Interscience, USA*, 1988.
70. A. Dörr, A. Sadiki and A. Mehdizadeh, *Journal of Rheology*, 2013, **57**, 743-765.
71. B. D. Cullity and C. D. Graham, *Introduction to Magnetic Materials*, Wiley-IEEE Press, 2008.
72. K. Stephan, *Analog and mixed-signal electronics*, John Wiley & Sons, 2015.
73. H. Saotome and Y. Sakaki, *IEEE Transactions on Magnetics*, 1997, **33**, 728-734.
74. W. Y. Du, *Resistive, capacitive, inductive, and magnetic sensor technologies*, CRC Press, 2014.
75. M. C. D. Lazarus N., *Materials Research Express*, 2016, **3**, 10.
76. A. Nadernezhad, N. Khani, G. A. Skvortsov, B. Toprakhisar, E. Bakirci, Y. Menciloglu, S. Unal and B. Koc, *Scientific reports*, 2016, **6**, 33178.
77. N. Khani, A. Nadernezhad, P. Bartolo and B. Koc, *CIRP Annals-Manufacturing Technology*, 2017.

## Chapter 6 Experimental Section

### 6.1 Materials

Iron (II, III) oxide nanoparticles (50–100 nm, 97%), Acrylic acid (AA 99%), N-[3(dimethylamino)propyl] methacrylamide (DMAPMA), and potassium peroxydisulfate (KPS,  $\geq 99.0\%$ ) were supplied from Sigma-Aldrich. Poly(ethylene glycol) (PEG, MW=1000 g mol<sup>-1</sup>) and maleic anhydride (MA, 99 %) were obtained from Merck. All the chemicals were used without further purification. All the solutions were prepared using distilled water with resistivity of 18.2 M $\Omega$  cm. The enameled copper wires (with diameters of 0.2 and 0.3 mm) were purchased from Emtel Enamel Wire and Cable Industry Co., Turkey.

### 6.2 Synthesis and characterization of the additives

#### 6.2.1 Synthesis of the additives

Equimolar amounts of PEG-1000 and maleic anhydride were charged in a 250 ml three-neck flask and the reaction was heated up to 90 °C. The reaction medium was kept under nitrogen gas purging for 2 hours; then, cooled to the room temperature. We used this product referred to as PEGMA for the polymerization without any purification.

In a typical aqueous free radical polymerization of DMAPMA:AA:MAPEG with molar ratio of 25:25:1, 0.05 mole of DMAPMA, 0.05 mole of AA, and 0.002 mole of MAPEG (MW $\approx$ 1100 g mol<sup>-1</sup>) were dissolved in 100 ml of distilled water. Subsequently, we charged the mixture into a 250 ml three-neck flask connected to a reflux condenser. Under the nitrogen gas purging, while being magnetically stirred, the temperature of the mixture was raised to 50 °C. At 50 °C, 75 ml KPS (initiator) aqueous solution (1 mol. % of the total mole of the comonomers) was dropwise added to the reaction chamber in 10 min. The temperature of the reaction was increased to 70 °C, and thereafter, the reaction was continued for 12 hours. All the other additives were also synthesized through the same procedure by changing the molar ratio of the building blocks (see Table 1.1). Finally, we cooled the reaction down to room temperature, and the copolymers were precipitated in either ethanol or acetone and were dried under moderate vacuum at 60 °C for 24 hours.

## 6.2.2 Characterization of the additives

Chemical and structural characterization of copolymers was carried out by nuclear magnetic resonance (NMR, Varian Unity Inova 500MHz spectrometer).

Density of anionic sites of the copolymers were determined by titration method with a HI-2211 bench top pH meter on 50 ml solution of 1 mg/ml copolymer/water at  $22 \pm 2$  °C. Copolymer solutions were titrated with a 0.1 M NaOH.

Copolymers were characterized by gel permeation chromatography (GPC, Agilent 1260 Infinity equipped with refractive index detector) in aqueous solution of 0.14 mol/l NaCl, 0.01 mol/l Na<sub>2</sub>HPO<sub>4</sub> and 0.01 mol/l NaNO<sub>3</sub> at a flow rate of 0.7 ml/min.

## 6.3 Preparation and 3D printing of highly-loaded iron oxide inks

### 6.3.1 Ink formulation

Throughout the experiments, we first dissolved the copolymers in 25 g of distilled water, then suspended the IOPs in these solutions through mechanical stirring. Portions of 2 g of IOPs were slowly added to the initial solution of the copolymer and the mixture was mechanically stirred for 15 min. Then, at 5-minute intervals, 2 g of IOPs were further added to the mixture to reach the target solid content. The mechanical stirring of the mixture was continued for further 24 hours at 400 rpm. 1 g of inks with a 5-mL syringe was taken and immediately was placed in a moisture analyzer (Shimadzu uniBloc MOC63u) to measure its solid content—the solid contents that are listed in this study are based on these measurements.

### 6.3.2 3D printing of highly-loaded iron oxide inks

Magnetic cores were 3D printed with the use of the ink containing ~81 wt. % of IOPs in the presence of 1.15 wt. % of P10 through custom-made 3D printer (SU<sup>3D</sup>) (Figure S6). More details about the hardware of this equipment can be found elsewhere.<sup>76, 77</sup> The cores were printed on a glass substrate pneumatically with the speed of 10 mm s<sup>-1</sup> through a nozzle of 510 μm diameter.

### 6.3.3 Electro-kinetic study and adsorption behavior of the additives

A Zeta potential analyzer (Zetasizer nanoseries, Malvern Instruments, Ltd.) equipped with a 633 nm laser and scattered light detector at a constant angle of 173° was employed to record the electro-kinetic behavior of IOPs in the presence of different amounts of the additives employing Smoluchowski approximation. The suspensions with 1 mg of IOPs in 100 mL of distilled water were ultrasonicated for 5 min in a bath sonicator. Then, certain amounts of the solutions of the additives were added to the suspensions of IOPs, and these mixtures were ultrasonicated for 5 min. Finally, the mixtures were stirred mechanically for a further 10 min. Six measurements with at least 15 runs were conducted at 25 °C and the average values of them were reported.

Adsorption behaviors of the additives were investigated via thermogravimetric analysis (TGA) (Netzsch STA 449C Jupiter thermal analyzer). All suspensions were prepared by 10 min ultrasonication of 0.5 g of IOPs in 40 g of distilled water that contained different amounts of the additives. These suspensions were further mechanically stirred for 15 min. Thereafter, the mixtures were centrifuged at 5000 rpm for 30 min. The sediments were then dispersed again in distilled water and were centrifuged again for another 30 min at 5000 rpm. Afterwards, the sediments were collected and dried at 60 °C for 24 h. The dried samples of ~ 40 mg were heated up under air atmosphere from room temperature to 800 °C with the heating rate of 10 °C min<sup>-1</sup>. The amounts of the adsorbed additives were measured by comparing the weight loss of the samples with that of the bare IOPs under the same thermal conditions. Each point of the adsorption graph is the average of at least three measurements (error deviation of the results of the measurements were ±0.05 wt. %).

### 6.3.4 Rheological study

The rheological measurements were performed with an Anton-Paar MCR 302 rheometer with parallel plates of 25 mm diameter and a gap size of 0.5 mm. After loading of each sample, a thin layer of low-viscosity paraffin oil was employed to protect the samples from adsorption of humidity at the outer edges of the plates. In dynamic regime, the frequency was set to 10 rad s<sup>-1</sup> and the strain was changed from 0.01 to 1000 % to find the range of the linear viscoelastic region. In steady-state tests, the shear rate ranged from 0.01 to 100 s<sup>-1</sup>.

### **6.3.5 Potentiometric titration of the solutions of the additives**

Potentiometric titration was conducted with a HI-2211 bench top pH meter on 50 ml solution of 1 mg.ml<sup>-1</sup> additives/water at 22 ± 2 °C. The pH of the solutions was adjusted by a 0.1 M HCl solution and then they were titrated with a 0.1 M NaOH solution.

### **6.3.6 Studying the interaction of the additives with Fe<sup>3+</sup> Ions**

To investigate the interaction of the additives with Fe<sup>3+</sup> ions, ICP-OES (Varian, Vista-pro) was used through a method that was reported elsewhere.<sup>64</sup> In a typical sample preparation, 15 ml aqueous 1 mg/ml solutions of the additives containing 0.001 mol of Fe<sup>3+</sup> ions were prepared. After 30 minutes of magnetic stirring, 5 ml of 1 M NaOH solution was added dropwise to the mixture of the additives and Fe<sup>3+</sup> ions to precipitate the free Fe<sup>3+</sup> ions from the solution. The mixtures were then centrifuged at 5000 rpm for 30 min and the supernatant was separated from the brownish-colored precipitate. Thereafter, the Fe<sup>3+</sup> concentration in the supernatant was measured by ICP-OES (Table 1.2).

### **6.3.7 Field emission scanning electron microscopy (FESEM)**

The morphologies of the outer surface and the fractured surface of the printed structures were analyzed by FESEM using a Leo Supra 35VP FESEM at a working distance of 8 mm and an accelerating voltage of 4 kV. All samples were coated with platinum before the measurements.

### **6.3.8 Impedance spectroscopy**

The electrical behavior of the enameled copper wire-wound printed cores was investigated using an impedance analyzer (Solartron analytical 1260, Impedance/Gain Phase Analyzer). The inductors were connected to the impedance analyzer and their inductance and resistance were recorded while sweeping the frequency from 0.1 to 10 MHz. The initial voltage of 1V was applied for all the measurements.

### **6.3.9 Magnetic characterization**

Magnetic properties of the bare IOPs and the dried powder form of the ink used for the 3D printing were measured by an in-house developed vibrating sample magnetometer (VSM) under a maximum applied magnetic field of 11 kOe at ambient temperature.